Physics-Based Band Gap Model for Relaxed and Strained [100] Silicon Nanowires

Ram Krishna Ghosh, Sitangshu Bhattacharya, and Santanu Mahapatra, *Senior Member, IEEE*

***Abstract*—In this paper, we propose a physics-based simplified analytical model of the energy band gap and electron effective mass in a relaxed and strained rectangular [100] silicon nanowires (SiNWs). Our proposed formulation is based on the effective mass approximation for the nondegenerate two-band model and 4×4 Lüttinger Hamiltonian for energy dispersion relation of conduction band electrons and the valence band heavy and light holes, respectively. Using this, we demonstrate the effect of the uniaxial strain applied along [100]-direction and a biaxial strain, which is assumed to be decomposed from a hydrostatic deformation along [001] followed by a uniaxial one along the [100]-direction, respectively, on both the band gap and the transport and subband electron effective masses in SiNW. Our analytical model is in good agreement with the extracted data using the extended-Hückel-method-based numerical simulations over a wide range of device dimensions and applied strain.**

***Index Terms*—Band gap, effective mass, nanowires, size quantization, strain.**

I. Introduction

SILICON NANOWIRE (SiNW) has emerged as a building block for the next-generation nanoelectronic devices as it can accommodate multiple-gate transistor architecture with excellent electrostatic integrity. However, as the experimental extraction of its various energy band parameters at the nanoscale regime is an extremely challenging task, it is customary to adopt atomic level simulations, whose results are at par with the experimental data. Two such parameters are the band gap and effective mass, which are of pioneer importance for the understanding of the current transport mechanism.

In recent years, there has been an extensive investigation on the variation of band gap and electron effective mass along different channel orientations in both relaxed [1]–[4] and strained [5]–[7] SiNWs, which are based on numerical methods like the first principle, pseudopotential, semiempirical, etc. Although there exists a large number of empirical relations of the band gap in relaxed SiNW [4], [8], there is a growing demand for the development of a physics-based analytical model to standardize different energy band parameters, which particularly demands its application in TCAD software for predicting different electrical characteristics of novel devices like SiNW-based relaxed tunnel field effect transistors and its strained counterpart [9].

The main challenge involved in the formulation of the analytical method for these two parameters (i.e., the band gap and the effective masses) comes from the transition of the indirect energy band gap of bulk Si near X point of the Brillouin zone to direct energy band gap at Γ point of SiNW. Due to this, the direct energy band gap starts depending on the conduction subband effective masses at the Γ point, which, in turn, depends on the conduction and valence subband energies. This conduction subband energy is, again, dependent on the subband electron effective masses, thus making it a coupled relation. This results in a parallel variation of all the parameters of an intrinsic Si that are entangled to each other.

Thus, the major contributions of this work are listed as follows:

1) an analytical technique to estimate the band gap and electron effective mass in [100] SiNW;
2) formulation of electron effective masses at the quantized subband levels along the two confined directions, together with the transport effective mass under both relaxed and strained conditions.

We use a relaxed nonparabolic dispersion relation based on the effective mass approximation (EMA) for the conduction band in bulk Si near the X point and 4×4 Lüttinger Hamiltonian dispersion relation for valence band heavy holes (HH) and light holes (LH) to formulate the bulk electron effective mass along the three different directions x, y, and z and the hole energies, respectively. This is followed by the incorporation of the quantum confinement effects to generate the quantized subband energies at the Γ point of [100] SiNW to formulate the transport and subband electron effective masses and the direct energy band gap. Further, we apply a uniaxial strain followed by a hydrostatic one along [100]- and [001]-directions, respectively, to form a biaxial strain with the former one. Both the tensile and compressive strain is being associated with this uniaxial and biaxial strain. The analytical data of the band gap and the electron transport effective masses for both relaxed and strained rectangular SiNW are further being compared with the data extracted from the Atomistix ToolKit (ATK), which uses a semiempirical approach by taking the extended Hückel method [10]. Our analytical model stands valid for the cases where the strain are within 1% and the spin–orbit coupling does not influence the conduction energy band.

Manuscript received October 24, 2011; revised February 7, 2012; accepted March 7, 2012. Date of publication April 4, 2012; date of current version May 23, 2012. This work was supported by the Indian Institute of Science and Indian Space Research Organization, Space Technology Cell, India, under Grant ISTC/EED/SM/253. The review of this paper was arranged by Editor K. Roy.

The authors are with the Nano-Scale Device Research Laboratory, Department of Electronic Systems Engineering (formerly Centre for Electronics Design and Technology), Indian Institute of Science, Bangalore 560 012, India (e-mail: ramki.phys@gmail.com; isbsin@yahoo.co.in; santanu@cedt.iisc.ernet.in).

Color versions of one or more of the figures in this paper are available online at http://ieeexplore.ieee.org.

Digital Object Identifier 10.1109/TED.2012.2190737

II. Model and Discussions

A. Relaxed SiNW

An intrinsic relaxed bulk Si crystal consists of six equivalent conduction band minima located symmetrically along $\langle 100 \rangle$ at a distance of approximately $k_0 = 0.815(2\pi/a_0)$ from the Γ point along X line in a 3-D Brillioun zone, in which a_0 is the relaxed lattice constant of Si. The nonparabolic energy dispersion relation of the bulk conduction band electrons can then be written following the EMA formalism as [11]:

$$E(1+\alpha E) = \frac{\hbar^2}{2m_l}(k_z - k_0)^2 + \frac{\hbar^2 k_x^2}{2m_t} + \frac{\hbar^2 k_y^2}{2m_t} \qquad (1)$$

in which E is the electron energy as measured from the bottom of the conduction band minimum, $\hbar\,[=(h/2\pi)]$ is the reduced Planck's constant, $m_l\ (=0.91m_0)$ and $m_t(=0.19m_0)$ are the longitudinal and transverse electron effective mass, respectively, where m_0 is the free electron mass, $\alpha = 0.5\ (\text{eV})^{-1}$ is the nonparabolicity factor [11], and k_x, k_y, and k_z are the electron wave vectors along the x-, y-, and z-directions, respectively. At this point, it should be noted that this relation is isotropic in the (001) plane and fails to describe the conduction band wrapping and the subband structure correctly in (110)-oriented Si films [11], [12]. In particular, to correlate a complete analytical conduction band dispersion relation with the advanced empirical tight binding model like $sp^3d^5s^*$, a two-band degenerate $\mathbf{k}\cdot\mathbf{p}$ model should be used where a second conduction band close to the first conduction band must be taken into account, the two of which become degenerate just at the X point [11]. These are generally called as primed $(\triangle_{2\prime})$ and unprimed $(\triangle_1)$ bands, respectively. This phenomenon is, however, not arrested in the simple nonparabolic EMA relation as given in (1), but since the electron energy in a state of the art MOSFET is of few tenths of electron-volts [13] within which the energy diagram from (1) and the $sp^3d^5s^*$ are almost same [11], one can use (1) safely for a simplified analytical solution of the band gap and electron effective mass without affecting the electron transport mechanism.

Assuming that the spin–orbit interaction between the HH and LH with split-off holes is less, the hole dispersion relation at the Γ point can be written as [14]

$$E = Ak^2 \pm \left[B^2k^4 + C^2\left(k_x^2k_y^2 + k_y^2k_z^2 + k_z^2k_x^2\right)\right]^{1/2} \qquad (2)$$

where E in this case is the hole energy as measured from the top of the valence band maxima, $\pm$ indicates the HH and LH bands, $k^2 = k_x^2 + k_y^2 + k_z^2$ and $A = -(4.1 \pm 0.2)(\hbar^2/2m_0)$, $|B| = (1.6 \pm 0.2)(\hbar^2/2m_0)$, and $|C| = (3.3 \pm 0.5)(\hbar^2/2m_0)$ are the inverse mass band parameters.

The band structure of relaxed SiNW whose electron transport is along [100]-direction is an involved task. The $sp^3d^5s^*$ model exhibits the fact that the symmetry between the six equivalent conduction band minima is now displaced due to the difference in the effective mass as a result of the quantum confinement of the carriers along y- and z-directions. Because of this, the six conduction band valleys are now grouped in four in-plane (Δ_4) along y- and z-directions and two out-of-plane (Δ_2) valleys along the x-direction. The former is projected at the Γ point of the 1-D Brillioun zone, while the latter is zone folded to $k_x = \pm 0.37(\pi/a_0)$ [1], [15]. Due to the lighter electron effective mass in the Δ_4 valley, the corresponding energy minimum is at a lower position than that of the Δ_2 valley, thus making the NW to be a direct band gap. This chronological transition of the energy wave vector minimum from an indirect to a direct band gap as a result of the corresponding change from the bulk Si structure to its [100] NW depends not only on the effective masses at the band minima but also on to the subband energies along the confinement directions. Several numerical methods exhibit the fact that a [100]-oriented SiNW acts as a direct band gap material roughly below 4 nm diameter [8], [16], [17].To simplify this mathematical hierarchy and to correlate with the existing numerical models, without any loss of generality, we assume the following empirical relation between the wave vector minima of the NW and k_0 to be

$$k_{\min} = k_0\left\{1 + \exp\left[\eta\left(1 - \frac{(\pi/10a_0)^2}{k_zk_y}\right)\right]\right\}^{-1} \qquad (3)$$

where η can be assumed to be a constant (in this case, $\eta = 10$). As there is no conclusive experimental or simulation evidences of how, in general, $k_{\min}$ changes at this transition region leading to a direct from indirect band gap, the empirical model as given in (3) would be much helpful in understanding the mechanism of the behavior of the electron effective masses near this transition region.

As seen in Fig. 1(a) represents a schematic diagram of a [100]-oriented SiNW, the atomistic cross-sectional view along y and z of which is exhibited in Fig. 1(b). This has been carried out using the ATK simulator. After a cleaved [100] fully relaxed atomic configured SiNW, the dangling bonds on the Si surface are sp^3 passivated with hydrogen atoms to dissolve any surface states in the band gap region. We have considered the nearest Si–Si and Si–H bond lengths to be 0.235 and 0.152 nm, respectively [16]. For the band structure computation, we used the semiempirical extended Hückel method instead of the usual ATK-DFT method. This has been used due to two main reasons: first, the DFT calculation does not provide a good estimation of the energy band gap, and second, the extended Hückel approach is more computationally efficient with a simultaneous good convergence [18]. The Hückel basis set used for the computations included Cerda silicon (GW Diamond) [19] and Hoffman hydrogen having a vacuum energy level of -7.67 and 0 eV, respectively, with a Wolfsberg weighting scheme. The tolerance parameter was 10^{-5} with maximum steps of 100, and a Pulay mixer algorithm [20] was used as the iteration control parameter. In addition, the k-point sampling of $1 \times 1 \times 11$ grid was used with a mesh cutoff energy of 20 Hatree. In all the following subsequent sections, we have strictly maintained the same aforementioned control parameters. Fig. 1(c) exhibits the energy band structure of the [100] SiNW for a square cross section of width 1.5 nm. It can be seen in Fig. 1(c) that using the Hückel basis set, the lifting of the valley degeneracy due to the difference in electron effective mass is not captured, which has already been stated earlier. However, as the valley splitting energy even in room temperature is relatively small in [100] and [001] SiNWs, one can ignore its contribution to the

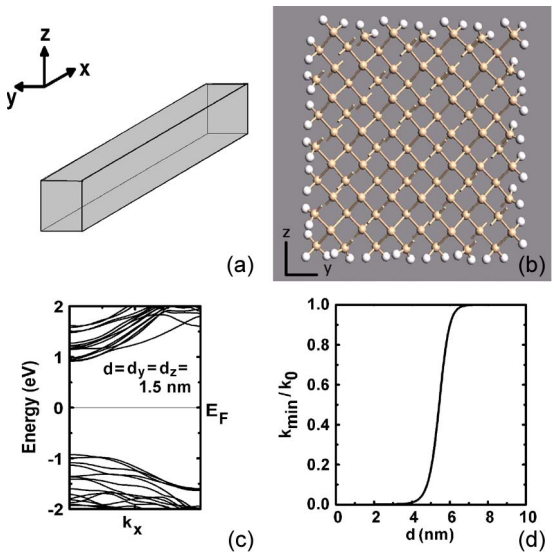

Fig. 1. (a) Schematic of the [100]-oriented channel of SiNW with cross-sectional thicknesses d_y and d_z along the y- and z-directions, respectively. (b) ATK built an sp^3 hydrogen passivated (100) SiNW plane. (c) Energy band structure of a [100] hydrogen passivated SiNW of square cross-sectional area using ATK builder that uses an extended Hückel approach. (d) Plot of $(k_{\min}/k_0)$ as function of thickness for a square cross-sectional SiNW. It appears that roughly below 4 nm, the conduction energy band minima for SiNW tends to Γ point. The role of η in this case is to make the curve continuous over the NW width.

modification of the carrier transport mechanism [1], [3], [21]. Further, as the band gap for a 1.5-nm-wide SiNW exhibited as a direct one, one can ignore this lifting of the valley degeneracy for the present relaxed case and can concentrate on the lowest valley at the Γ point that essentially determines the band gap. Fig. 1(d) represents the variation of $k_{\min}$ as a function of wire width for a square cross section that resembles much like the statistical Fermi–Dirac distribution function of holes at a finite temperature, where $k_{\min}$ dies out below roughly 4 nm, while above this, it rises quickly to its bulk value minima at k_0.

The use of (3) in (1) results the nonparabolic electron dispersion relation in [100] SiNW with NW electron effective masses m_x, m_y, and m_z as

$$E(1+\alpha E) = \frac{\hbar^2}{2m_z}(k_z - k_{\min})^2 + \frac{\hbar^2 k_x^2}{2m_x} + \frac{\hbar^2 k_y^2}{2m_y}. \quad (4)$$

Since the carriers about the Fermi energy only takes part in the conduction mechanism, the transport effective mass m_x, defined as

$$m_x = \hbar^2 \left(\frac{\partial^2 E}{\partial k_x^2}\right)^{-1}\Bigg|_{E=E_F} \quad (5)$$

should be evaluated when $E = E_F$ at the band minimum. In case of an intrinsic SiNW, the Fermi energy position is nearly at the middle of the band gap, thus, one can use $E_F \sim (E_{g_{\rm NW}}/2)$, where $E_{g_{\rm NW}}$ is the energy band gap of the SiNW for a particular thickness. The subband electron effective masses along the y- and z-directions, however, depends on the subband energies along their respective directions and are the solution for $E = E_n$ of (4) when the transport direction wave vector $k_x = 0$. It should be particularly noted that for the present analyses, we have not considered the effect of quantum confinement of the carriers in the set of (011) planes on the nonparabolicity factor α. Although this has been modeled recently for ultrathin Si films using two-band degenerate perturbation $\mathbf{k}\cdot\mathbf{p}$ theory, but leads to unsatisfactory results below certain film thickness [22]. The question of this band nonparabolicity factor has also been dealt by Wang *et al.* [3] for SiNWs where they took α to be a fitting parameter to correlate with their data. However, in the present analytical formalism, we have taken the theoretical value of α to be 0.6 $(\text{eV})^{-1}$ [11], a result close to 0.5 $(\text{eV})^{-1}$ as stated earlier.

Using (4) and (5), the transport effective electron mass m_x for [100] relaxed SiNW can be obtained as

$$m_x = (1 + \alpha E_{g_{\rm NW}}) m_t. \quad (6)$$

Equation (6) is the result of the assumption that the carriers obey the periodic Bloch waves together with the van Hove singularity conditions occurring due to the carrier confinement along the y- and z-directions. Under such "particle-in-a-box" conditions, we have $k_y = n_y\pi/d_y$ and $k_z = n_z\pi/d_z$, where d_y and d_z are the thicknesses of the SiNW and n_y and n_z are the quantum wire subband index numbers (1, 2, 3, ...) of the conduction subbands along the respective directions. Thus, we see that the transport effective mass along [100] of a relaxed SiNW depends on the corresponding energy band gap. However, it should be noted that for bulk relaxed Si crystal, (6) converges to $m_x = (1 + \alpha E_g) m_t \sim 0.32 m_0$, where $E_g = 1.12$ eV is the indirect band gap. Under the usual parabolic energy dispersion relation $(\alpha \to 0)$, and thus, $m_x = m_t = 0.19 m_0$. The subband effective mass along the y- and z-directions can, respectively, be written using (4) and (5) as

$$m_y = \frac{(1+2\alpha E_n)}{\left[1 - 2\alpha\left\{\frac{\hbar^2\left(\frac{n_y\pi}{d_y}\right)^2}{m_t(1+2\alpha E_n)^2}\right\}\right]} m_t \quad (7)$$

$$m_z = \frac{(1+2\alpha E_n)}{\left[1 - 2\alpha\left\{\frac{\hbar^2\left(\frac{n_z\pi}{d_z} - k_{\min}\right)^2}{m_l(1+2\alpha E_n)^2}\right\}\right]} m_l \quad (8)$$

in which E is replaced by E_n, which are the subband energies that can, in turn, be written using (4) as

$$E_n = \frac{1}{2\alpha}\left[-1 + \left\{1 + 4\alpha\left(\frac{\hbar^2}{2m_y}\left(\frac{n_y\pi}{d_y}\right)^2 + \frac{\hbar^2}{2m_z}\left(\frac{n_z\pi}{d_z} - k_{\min}\right)^2\right)\right\}^{\frac{1}{2}}\right]. \quad (9)$$

It appears from (7) and (8) that the subband effective masses along the confinement directions depends on the corresponding quantum numbers n_y and n_z. However, it is customary to assume that almost all the carriers are occupied within the lowest subbands for which $n_y = n_z = 1$. Physically, the energy band gap of 1-D nanowire is the absolute energy difference between the lowest conduction $(n_y = n_z = 1)$ and lowest valence

subband level ($m_y = m_z = 1$). Thus, using (7)–(9), the band gap for the relaxed SiNW can be written as

$$E_{g_{\rm NW}} = E_g + E_n|_{k_{\min}=0} + |E_p| \tag{10}$$

which is the absolute sum of its bulk value E_g, E_n evaluated at $k_{\min} = 0$ and $n_y = n_z = 1$ and E_p evaluated at $m_y = m_z = 1$, respectively, where E_p is the hole subband energy given by

$$E_p = A\left[\left(\frac{m_y\pi}{d_y}\right)^2 + \left(\frac{m_z\pi}{d_z}\right)^2\right] \pm \left[B^2\left[\left(\frac{m_y\pi}{d_y}\right)^2 + \left(\frac{m_z\pi}{d_z}\right)^2\right]^2 + C^2\left(\frac{m_y\pi}{d_y}\right)^2\left(\frac{m_z\pi}{d_z}\right)^2\right]^{1/2} \tag{11}$$

in which m_y and m_z are the hole subband index numbers (1, 2, 3, ...) of the split HH and LH valence bands along the respective directions. It also appears that due to the occurrence of the square root in (2), the HH and LH dispersion relation, in general, cannot be described by the effective masses [11]. Keeping this in view, we assume that the Lüttinger parameters A, B, and C are independent of the cross-sectional dimensions. It should be noted that E_g in (10) is the bulk indirect band gap value. However, the contribution to the band gap due to the thickness reduction comes directly from $E_n|_{k_{\min}=0}$ and E_p. This $E_n|_{k_{\min}=0}$ consists of the effective masses m_y and m_z through (7) and (8), which depends again on E_n in (9). Since $k_{\min}$ changes from its bulk position at k_0 to Γ, which leads to a corresponding change in the masses m_y and m_z, the band gap $E_{g_{\rm NW}}$ becomes a direct one. As the cross-sectional dimension increases, both the subband energies $E_n|_{k_{\min}=0}$ and E_p diminish, and $E_{g_{\rm NW}}$ tends to its indirect value E_g, which is essentially the difference between the conduction band minima and valence band maxima, where the bulk conduction band minima at k_0 comes implicitly in the EMA formulation.

Thus, we see that (6)–(10) are coupled equations, which cannot be solved directly. Furthermore, a parallel evaluation of various size-dependent parameters usually makes the analyses a formidable one to make any precise analytical formulation. Approximations are thus needed to obtain analytical and meaningful results. Hence, we first solve the subband energies using the relation given in (9) for the bulk effective masses m_l and m_t as

$$E^1 = \frac{1}{2\alpha}\left[-1 + \left\{1 + 4\alpha\left(\frac{\hbar^2}{2m_t}\left(\frac{\pi}{d_y}\right)^2 + \frac{\hbar^2}{2m_l}\left(\frac{\pi}{d_z} - k_{\min}\right)^2\right)\right\}^{\frac{1}{2}}\right] \tag{12}$$

where the subband effective mass are then evaluated from (7) and (8) as

$$m_y^1 = (1 + 2\alpha E^1)m_t \tag{13}$$

$$m_z^1 = (1 + 2\alpha E^1)m_l \tag{14}$$

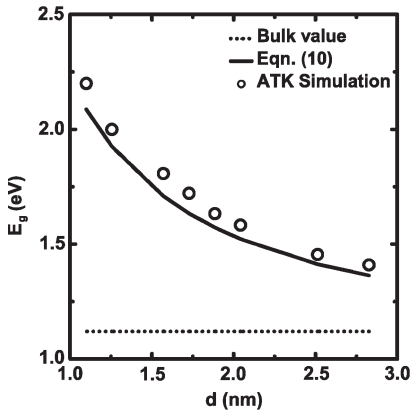

Fig. 2. Plot of the band gap using (10) in relaxed [100] SiNW as a function of lateral wire width $d_y = d_z = d$. The subband effective masses in (9) has been evaluated by using (16) and (17). The symbols are our simulation data that have been obtained by using the ATK by passivating the Si atoms at the surface of the wire using hydrogen atoms as shown in Fig. 1(b) followed by the use of semiempirical extended Hückel method.

in which we have neglected the denominator since the contribution of the factors $2\alpha\{(\hbar^2(\pi/d_y)^2/m_t(1 + 2\alpha E^1)^2)\}$ and $2\alpha\{(\hbar^2((\pi/d_z) - k_{\min})^2/m_l(1 + 2\alpha E^1)^2)\}$ are very less above 1 nm wire width. Using (13) and (14), we evaluate a more precise subband energy E^2 as

$$E^2 = \frac{1}{2\alpha}\left[-1 + \left\{1 + 4\alpha\left(\frac{\hbar^2}{2m_y^1}\left(\frac{\pi}{d_y}\right)^2 + \frac{\hbar^2}{2m_z^1}\left(\frac{\pi}{d_z} - k_{\min}\right)^2\right)\right\}^{\frac{1}{2}}\right] \tag{15}$$

where the subband effective mass generated from (15) can then be evaluated following (13) and (14) as

$$m_y^2 = (1 + 2\alpha E^2)m_t \tag{16}$$

$$m_z^2 = (1 + 2\alpha E^2)m_l. \tag{17}$$

Finally, replacing m_y and m_z by m_y^2 and m_z^2, respectively, in (9), and using (10), we find the SiNW direct band gap $E_{g_{\rm NW}}$. Fig. 2 exhibits the variation of [100] relaxed SiNW band gap as function of wire width of equal thickness. The effect of the carrier confinement along the [001]- and [010]-directions leads to the discrete subband energy levels for both the electrons and holes. In case of valence bands, the HH and LH form separate energy subband levels due to the difference in their energy. Thus, using this, it appears that the first subband of E_p for HH in a 1.5×1.5 nm^2 SiNW is about 0.1 eV below compared to that of the maxima point of the HH in case of bulk. However, for the LH subband, E_p is about 2.2 eV below the same. Thus, we see that the energy band gap difference in case of SiNW should be considered from the lowest conduction subband to the lowest HH subband, which is precisely meant by (10). Using (6), (16) and (17), Fig. 3 exhibits the variations of the transport and subband effective mass as a function of wire width. It appears that m_x decreases with the increase in width, and as $d \to \infty$, m_x tends to its nonparabolic bulk value, which is 0.32 m_0. In case of subband effective mass,

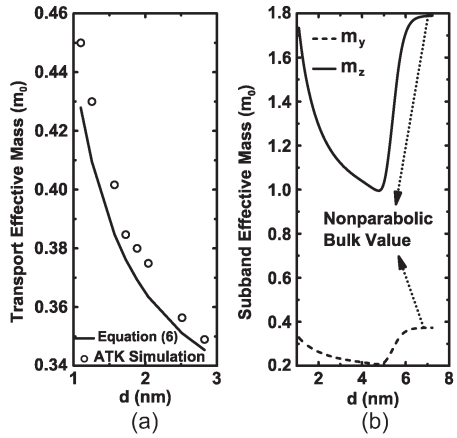

Fig. 3. Plot of the electron (a) transport effective mass using (6) and (b) subband effective mass using (16) and (17) as a function of wire thickness. The symbol represents the extracted data from the energy band structure obtained using ATK simulation.

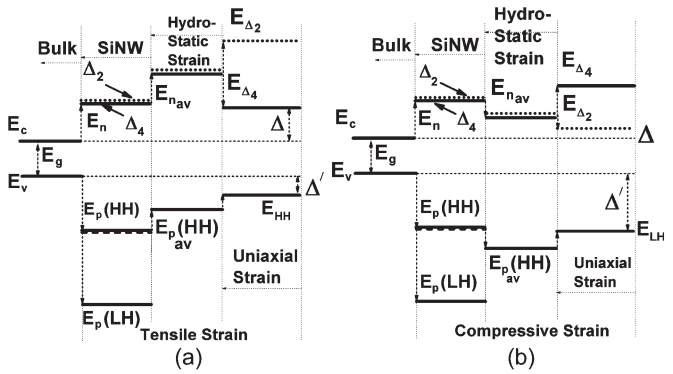

Fig. 4. Band alignment of the first ($n_y = n_z = m_y = m_z = 1$) conduction and valance subband using the EMA formulation under an application of a biaxial strain on [100] SiNW for (a) tensile and (b) compressive strain. Δ_2 and Δ_4 in relaxed SiNW are the results of difference in effective masses due to quantum confinement as arrested by the $sp^3d^5s^*$ method. The average of the HH and LH subband (as shown by the horizontal dotted line below E_p(HH) is assumed to coincide with the E_p(HH) for both the tensile and compressive cases due to higher effective mass of the former.

the variation is divided into two parts. Roughly below 5 nm, it appears that both m_y and m_z increase with a decrease in wire thickness. This is due to the reason that the contribution of $k_{\min}$ in (3) diminishes. Fig. 3(b), if compared with Fig. 1(d), exhibits that using our model (3), the direct-to-indirect transition occurs roughly below 4 nm. However, due to the addition of the term $((\pi/d_z) - k_{\min})$, the minimum of m_y and m_z is shifted to roughly about 5 nm. As the thickness increases, both the subband masses start increasing and reach their corresponding nonparabolic bulk effective masses, which are precisely $0.38m_0$ and $1.81m_0$, respectively. It should be noted that these bulk values are measured with respect to the valence band maxima at Γ point. However, if the origin is shifted to k_0, the value of these masses converges to $0.19m_0$ and $0.91m_0$, respectively.

Using this approach, the maximum error between our formulation and simulation data are within 3%. The main reason behind this error is due to the complete negligence of the spin–orbit interaction between the split-off holes and HH/LH in our model. The other part of the error comes due to the omission of the interaction of the plane waves of Hydrogen on the Si atoms due to which the band structure of ultrasmall thin SiNW gets affected. Our analytical model can also be compared to the band gap of circular SiNW under identical conditions. However, for other different cross-sectional shapes like circular and triangular [100] SiNW, the band gap exhibits almost zero deviations from each other when plotted against the cross-sectional area, whereas if plotted against cross-sectional dimension, both the transport effective mass and band gap exhibit slight deviations [3], [23].

B. Strained SiNW

The influence of strain on bulk Si crystal has different effects along different directions and has been extensively studied in past few decades [24], [25]. Recently, using the density functional theory, the effect of both uniaxial and biaxial strain on the band structure of a [100]-oriented SiNW has been shown, where the modification of the positions of already lifted Δ_4 and Δ_2 valleys due to the quantum confinement effects has been considered [7]. For our present quantitative analysis, we take into consideration a uniaxial and hydrostatic strain along the [100]- and [001]-directions, respectively. Fig. 4 schematically exhibits this situation on the conduction and valence bands for both tensile [Fig. 4(a)] and compressive [Fig. 4(b)] strains on a [100]-oriented SiNW. In case of a bulk Si, an application of a tensile hydrostatic strain shifts up the average energy of the conduction band with respect to its six equivalent valleys. In addition, a uniaxial strain along [100] splits this conduction band into Δ_2 and Δ_4. The position of these valleys about their bulk relaxed value, however, strictly depends whether the strain is tensile or compressive. For example, in a $\langle 110 \rangle$ uniaxial tensile strain, the position of Δ_4 is higher in energy than Δ_2 [26].

As shown in Fig. 4(a) for a relaxed SiNW, the two valleys Δ_4 (lower in energy) and Δ_2 (higher in energy) are the set of subbands as a result of $k_y = n_y\pi/d_y$ and $k_z = n_z\pi/d_z$. The average energy of this set of subbands under a tensile hydrostatic strain along [001] shifts up by the same amount. However, the presence of a uniaxial compressive strain along the [100]-direction makes Δ_4 to be higher in energy than that of Δ_2 [7], as shown in Fig. 4(b). In case of valence bands, the HH and LH split as subband energy levels [see (11)] in which a tensile hydrostatic strain shifts up their respective average position, while a uniaxial tensile strain shifts up the HH subbands over LH subbands [Fig. 4(a)]. We now discuss a quantitative analysis of the energy band gap and transport and subband effective masses under the presence of a biaxial strained [100] SiNW based on the EMA formalism as stated earlier. Further, in case of the split valence bands, we assume that the average position of the HH and LH subband almost coincides with the HH subband due to the higher effective mass of the former. The isotropic hydrostatic strain shifts the average energy of the nanowire conduction band edge from E_n [in (9) with $n_y = n_z = 1$] by an amount $E_{n_{\rm av}} = a_c(2\varepsilon/(1-\nu))$, where ε is the isotropic strain component. In addition, the influence of a uniaxial strain along [100] increases the difference in energy between the Δ_2 and Δ_4 subbands.

Each of these valleys now shifts by an amount $E_{\triangle_2} = (2/3)b_c(\varepsilon_{zz} - \varepsilon_{xx}) = (2/3)b_c((3\nu - 1)/(1 - \nu))\varepsilon$ and $E_{\triangle_4} = -(1/3)b_c(\varepsilon_{zz} - \varepsilon_{xx}) = -(1/3)b_c((3\nu - 1)/(1 - \nu))\varepsilon$, as shown in Fig. 4(a) and (b) with respect to their unstrained positions, where $\varepsilon_{zz} > 0$ and ε_{xx} are the strain tensor coefficient along the z- and x-directions, respectively. The parameters $a_c = 4.18$ eV and $b_c = 9.16$ eV are the deformation potentials for the hydrostatic and uniaxial strain in the Si conduction bands, respectively [24], [27], while $\nu = 0.37$ is the SiNW Poisson's ratio [28]. In case of the valence subbands, the hydrostatic strain shifts the average energy of the nanowire valence band edge from E_p [in (11) with $m_y = m_z = 1$] by an amount $E_{p_{\rm av}} = a_v(2\varepsilon/(1 - \nu))$. This is further shifted to an amount $E_{\rm LH} = 2b_v((3\nu - 1)/(1 - \nu))\varepsilon$ and $E_{\rm HH} = -b_v((3\nu - 1)/(1 - \nu))\varepsilon$ in case of tensile and compressive case, respectively, in which $a_v = 2.46$ eV and $b_v = -2.35$ eV are the valence band deformation potentials [24], [27]. Thus, we see from the energy band diagram in Fig. 4(a), that the band gap in a biaxially tensile strained [100] SiNW is given by

$$E_g(\varepsilon > 0) = E_g + \triangle + \triangle' \tag{18}$$

in which $\triangle = E_n|_{n_y=n_z=1} + E_{n_{\rm av}} + E_{\triangle_4}$, where $E_{n_{\rm av}}$ and $E_{\triangle_4}$ are positive and negative quantities and $\triangle' = |E_p|_{m_y=m_z=1}| - (E_{p_{\rm av}} + E_{\rm HH})$ in which $E_{p_{\rm av}}$ and $E_{\rm HH}$ are both positive quantities, respectively. In case of a compressive biaxial strain, (18) can be written following Fig. 4(b) as

$$E_g(\varepsilon < 0) = E_g + \triangle + \triangle' \tag{19}$$

where, in this case, $\triangle = E_n|_{n_y=n_z=1} + E_{n_{\rm av}} + E_{\triangle_2}$ in which $E_{n_{\rm av}}$ and $E_{\triangle_2}$ are both negative quantities and $\triangle' = |E_p|_{m_y=m_z=1}| - (E_{p_{\rm av}} + E_{\rm LH})$, where $E_{p_{\rm av}}$ is a negative quantity while $E_{\rm LH}$ is a positive one.

The effect of strain on the band gap in [100] SiNW has been exhibited in Fig. 5. It appears that band gap decreases as the uniaxial tensile and compressive strain increases, however, the rate of decrement is different due to the difference in energy between $E_{n_{\rm av}}$, $E_{p_{\rm av}}$, $E_{\rm LH}$, and $E_{\rm HH}$ in both the regime. It should be noted that an increase in the tensile strain decreases the energy of Δ_4 subbands, while the HH subbands shifts toward the valence band maxima position of the bulk Si. This marks a reduction of the band gap as the tensile strain increases. In case of uniaxial compressive strain, it is the Δ_2 that shifts down and LH shifts up, thus decreasing the band gap. The scenario changes when the uniaxial strain is combined with the [001] hydrostatic strain. Under this biaxial strain condition, the band gap increases along the tensile strain while decreases with compressive strain at a rate much faster than that of the corresponding uniaxial case. It is now well understood that the $sp^3d^5s^*$ model predicts the direct to indirect transition of the band gap in a $\langle 100 \rangle$ uniaxially strained SiNW occurring inside the compressive zone [7], [29]. The reason for this is the asymmetric splitting of the six equivalent valleys in bulk Si into Δ_4 and Δ_2 due to the quantum confinement of the carriers in SiNW. Since Δ_4 lies lower at the Γ point axis than Δ_2, which lies at higher energy at the off-Γ axis, it takes a certain amount of compressive strain to bring the Δ_2 subband (at the same off-Γ axis) lower than the Δ_4. Since this confinement splitting is not arrested in EMA formalism, Fig. 5 exhibits that the band gap from the beginning of the compressive strain starts becoming indirect. However, an increase in the tensile strain decreases the Δ_4 subband at the same Γ axis, whereby the band gap remains direct always.

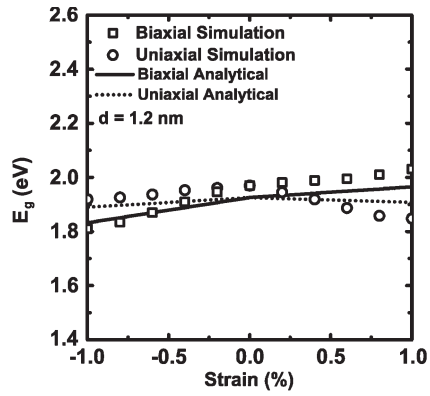

Fig. 5. Band gap as function of uniaxial strain along the [100]-direction and biaxial strain for the [100]-oriented SiNW. Symbols are the results of the ATK simulations.

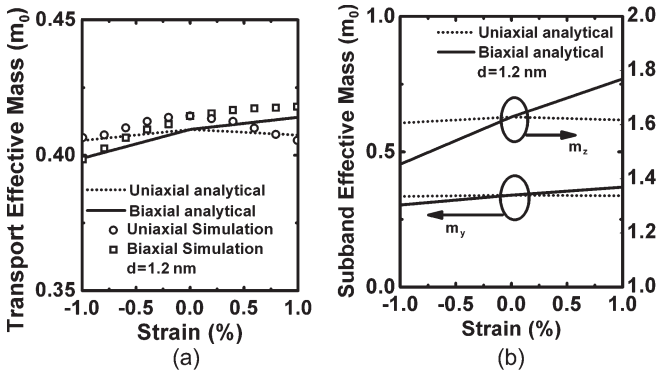

Fig. 6. Plot of the electron (a) transport effective mass and (b) subband effective mass as function of uniaxial and biaxial strain. The symbol represents the extracted data from the energy band structure obtained using ATK simulation.

The variation of the transport and subband effective mass as function of strain has been exhibited in Fig. 6 in which the transport effective mass is given as $m_x = (1 + \alpha E_g(\varepsilon))m_t$ and the subband effective masses at the first subband are given as $m_y = (1 + \alpha\triangle)m_t$ and $m_z = (1 + \alpha\triangle)m_l$. It appears from Fig. 6(a) that with the increase in both uniaxial tensile and compressive strain, the transport effective mass follows the same rate of decrement as exhibited by its corresponding band gap variation. However, in the case of subband effective mass as seen in Fig. 6(b), the variation follows Δ. It appears that the subband effective mass along the z-direction has larger variation due to the application of the hydrostatic strain than that of the y-direction. Further above 0 strain, the effective masses are due to the direct band gap, and below 0 strain, the effective masses are due to the indirect band gap, a reason that has already been stated earlier.

Finally, the work, as exhibited here, lightens an analytical method of extracting these parameters through in an iterative way until the solutions converge. Although it is not possible to decouple the entangled relation between the band gap and

effective electron masses along different directions, however, our analytical approach lies with the easier and reduced steps with an excellent convergence in extracting these energy band parameters by considering the effects of quantum confinement. Further, in defining (3), it should be noted that (3) is independent of strain since strain changes the electron energy levels not the minima points as long as nanowires are concerned [7], [11]. We wish to state that the methods as presented in this work for the formalism of both the band gap and effective mass in the presence of strain may be useful for the determination of different electrical transport properties in uniaxial ([110]-direction) and biaxially ([110] and [001]) strained [110] SiNWs. The results and the methodologies as carried out in this work can be tuned further by modifying the nanowire dispersion relation by considering the variation of the nonparabolicity factor as a function of film thickness and incorporating the valley splitting, which would certainly increase the accuracy of our analytical results, although the qualitative features of the band gap and the effective masses both in relaxed and strained case would not change.

III. Conclusion

In this paper, we have presented an analytical technique to estimate the band gap and electron effective mass in a [100]-oriented relaxed and strained SiNW. Using this, we investigate the variation of the band gap and the effective mass along the transport direction and confined directions as function of cross-sectional dimension and applied strain. The results of our analytical model for both relaxed and strained SiNWs are in good agreement with that of the semiempirical extended Hückel method and found to possess an error less than 3%.

References

[1] N. Neophytou, A. Paul, M. S. Lundstrom, and G. Klimeck, "Bandstructure effects in silicon nanowire electron transport," *IEEE Trans. Electron Devices*, vol. 55, no. 6, pp. 1286–1297, Jun. 2008.

[2] E. Zheng, C. Rivas, R. Lake, K. Alam, T. B. Boykin, and G. Klimeck, "Electronic properties of silicon nanowires," *IEEE Trans. Electron Devices*, vol. 52, no. 6, pp. 1097–1103, Jun. 2005.

[3] J. Wang, A. Rahman, A. Ghosh, G. Klimeck, and M. S. Lundstrom, "On the validity of the parabolic effective-mass approximation for the I–V calculation of silicon nanowire transistors," *IEEE Trans. Electron Devices*, vol. 52, no. 7, pp. 1589–1595, Jul. 2005.

[4] J. A. Yan, L. Yang, and M. Y. Chou, "Size and orientation dependence in the electronic properties of silicon nanowires," *Phys. Rev. B*, vol. 76, no. 11, pp. 115 319-1–115 319-6, Sep. 2007.

[5] M. O. Baykan, S. E. Thompson, and T. Nishida, "Strain effects on three-dimensional, two-dimensional, and one-dimensional silicon logic devices: Predicting the future of strained silicon," *J. Appl. Phys.*, vol. 108, no. 9, pp. 092716-1–092716-24, Nov. 2010.

[6] R. N. Sajjad and K. Alam, "Electronic properties of a strained $\langle 100 \rangle$ silicon nanowire," *J. Appl. Phys.*, vol. 105, no. 4, pp. 044307-1–044307-6, Feb. 2009.

[7] K.-H. Hong, J. Kim, S.-H. Lee, and J. K. Shin, "Strain-driven electronic band structure modulation of Si nanowires," *Nano Lett.*, vol. 8, no. 5, pp. 1335–1340, May 2008.

[8] P. W. Leu, B. Shan, and K. Cho, "Surface chemical control of the electronic structure of silicon nanowires: Density functional calculations," *Phys. Rev. B*, vol. 73, no. 19, pp. 195 320-1–195 320-5, May 2006.

[9] International Technology Roadmap for Semiconductors. [Online]. Available: http://www.itrs.net/Links/2009ITRS/2009Chapters_2009Tables/2009_ExecSum.pdf

[10] Atomistix ToolKit (ATK), QuantumWise Simulator, [Online]. Available: http://www.quantumwise.com/

[11] V. Sverdlov, *Strain-Induced Effects in Advanced MOSFETs*. Wein, NY: Springer-Verlag, 2011.

[12] K. Uchida, A. Kinoshita, and M. Saitoh, "Carrier transport in (110) nMOSFETs: Subband structures, non-parabolicity, mobility characteristics, and uniaxial stress engineering," in *IEDM Tech. Dig.*, 2006, pp. 1019–1021.

[13] M. S. Lundstrom and J. Guo, *Nanoscale Transistors: Device Physics Modeling and Simulation*. New York: Springer-Verlag, 2006.

[14] G. Dresselhaus, A. F. Kip, and C. Kittel, "Cyclotron resonance of electrons and holes in silicon and germanium crystals," *Phys. Rev.*, vol. 98, no. 2, pp. 368–384, Apr. 1955.

[15] R. N. Sajjad, K. Alam, and Q. D. M. Khosru, "Parametrization of a silicon nanowire effective mass model from $sp^3d^5s^*$ orbital basis calculations," *Semicond. Sci. Technol.*, vol. 24, no. 4, pp. 045023-1–045023-8, Mar. 2009.

[16] M.-F. Ng, L. Zhou, S.-W. Yang, L. Y. Sim, V. B. C. Tan, and P. Wu, "Theoretical investigation of silicon nanowires: Methodology, geometry, surface modification, and electrical conductivity using a multiscale approach," *Phys. Rev. B*, vol. 76, no. 15, pp. 155 435-1–155 435-11, Oct. 2007.

[17] J.-B. Xia and K. W. Cheah, "Quantum confinement effect in thin quantum wires," *Phys. Rev. B*, vol. 55, no. 23, pp. 15 688–15 693, Jun. 1997.

[18] D. Kienle, K. H. Bevan, G.-C. Liang, L. Siddiqui, J. I. Cerda, and A. W. Ghosh, "Extended Hückel theory for band structure, chemistry, and transport—Part 2: Silicon," *J. Appl. Phys.*, vol. 100, no. 4, pp. 043715-1–043715-8, Aug. 2006.

[19] J. Cerda and F. Soria, "Accurate and transferable extended Hückel-type tight-binding parameters," *Phys. Rev. B*, vol. 61, no. 12, pp. 7965–7971, Mar. 2000.

[20] P. Pulay, "Convergence acceleration of iterative sequences the case of scf iteration," *Chem. Phys. Lett.*, vol. 73, no. 2, pp. 393–398, Jul. 1980.

[21] S. Jin, M. V. Fischetti, and T.-W. Tang, "Theoretical study of carrier transport in silicon nanowire transistors based on the multisubband Boltzmann transport equation," *IEEE Trans. Electron Devices*, vol. 55, no. 11, pp. 2886–2897, Nov. 2008.

[22] V. Sverdlov, H. Kosina, and S. Selberherr, "Electron subband dispersions in ultra-thin silicon films from a two-band $\mathbf{k} \cdot \mathbf{p}$ theory," *J. Comput. Electron.*, vol. 7, no. 3, pp. 164–167, Sep. 2008.

[23] R. N. Sajjad, S. Bhowmick, and Q. Khosru, "Cross-sectional shape effects on the electronic properties of silicon nanowires," in *Proc. IEEE EDSSC*, 2008, pp. 1–4.

[24] C. G. V. de Walle and R. M. Martin, "Theoretical calculations of heterojunction discontinuities in Si/Ge systems," *Phys. Rev. B*, vol. 34, no. 8, pp. 5621–5634, Oct. 1986.

[25] J. C. Hensel and G. Feher, "Cyclotron resonance experiments in uniaxially stressed silicon: Valence band inverse mass parameters and deformation potentials," *Phys. Rev.*, vol. 129, no. 3, pp. 1041–1062, Feb. 1963.

[26] Y. Sun, S. E. Thompson, and T. Nishida, *Strain Effect in Semiconductors: Theory and Device Applications*. Heidelberg, Germany: Springer-Verlag, 2010.

[27] P. Y. Yu and M. Cardona, *Fundamentals of Semiconductors: Physics and Materials Properties*., 4th ed. New York: Springer-Verlag, 2010.

[28] M. Durandurdu, "Ab initio modeling of small diameter silicon nanowires," *Phys. Stat. Solid (B)*, vol. 243, no. 2, pp. R7–R9, Feb. 2006.

[29] D. Shiri, Y. Kong, A. Buin, and M. P. Anantram, "Strain induced change of bandgap and effective mass in silicon nanowires," *Appl. Phys. Lett.*, vol. 93, no. 7, pp. 073114-1–073114-3, Aug. 2008.

Ram Krishna Ghosh received the B.Sc. degree in physics from the University of Calcutta, West Bengal, India, in 2006 and the M.Sc. degree in physics from the Indian Institute of Technology Madras, Chennai, India, in 2008. He is currently working toward the Ph.D. degree in the Nano Scale Device Research Laboratory, Department of Electronic Systems Engineering (formerly CEDT), Indian Institute of Science, Bangalore, India.

His research interests include the quantum transport in nanoscale semiconductor devices.

Sitangshu Bhattacharya received the B.S. and M.S. degrees from the University of Calcutta, West Bengal, India, in 2001 and 2003, respectively, and the Ph.D. degree from Jadavpur University, Calcutta, India, in 2009.

He is currently a Postdoctoral Young Scientist with the Department of Electronic Systems Engineering, Indian Institute of Science, Bangalore, India. His current research topic includes the theoretical modeling of electro-thermal transport properties in low dimensional structures and devices under external controlled fields.

Santanu Mahapatra (M'08–SM'10) received the Ph.D. degree from the Ecole Polytechnique Federale de Lausanne, Lausanne, Switzerland, in 2005.

He is currently an Associate Professor with the Indian Institute of Science, Bangalore, India. His research interests include compact modeling multigate transistors, carbon-based interconnects, and new materials for future nanoelectronics.

Dr. Mahapatra is the recipient of a Ramanna Fellowship from the Department of Science and Technology, Government of India.